Chinese Chemical Letters 35 (2024) 108406

Contents lists available at ScienceDirect

Chinese Chemical Letters

journal homepage: www.elsevier.com/locate/cclet

Highly uniform Co-Cu bimetallic sulfides for rechargeable alkaline aqueous zinc batteries

Xiaofang Bai[a,b,1], Yuwei Zhao[b,c,1], Mangwei Cui[b], Tianshuo Guo[a], Zijie Tang[b], Chuan Li[b], Heng Gao[d], Shuo Yang[b], Lingzhi Zhao[e], Chunyi Zhi[b,c], Hongfei Li[a,b,*]

[a] Department of Materials Science and Engineering, Southern University of Science and Technology, Shenzhen 518055, China
[b] Songshan Lake Materials Laboratory, Dongguan 523808, China
[c] Department of Materials Science and Engineering, City University of Hong Kong, Hong Kong, China
[d] International Centre for Quantum and Molecular Structures, Department of Physics, Shanghai University, Shanghai 200444, China
[e] Guangdong Provincial Engineering Technology Research Center for Low Carbon and Advanced Energy Materials, Institute of Semiconductor Science and Technology, South China Normal University, Guangzhou 510631, China

ARTICLE INFO

Article history:
Received 29 December 2022
Revised 15 February 2023
Accepted 29 March 2023
Available online 31 March 2023

Keywords:
Aqueous zinc batteries
Bimetallic sulfides
Cathode materials
Rate performance
Cycling stability

ABSTRACT

Rechargeable alkaline aqueous zinc batteries (RAZBs) have attracted increasing attention. However, most RAZBs are hindered by the limited availability of cathode materials. The practical electrochemical performance of most cathode materials is lower than the theoretical value due to their poor electrical conductivity and low utilization capacity. In this work, we develop a facile hydrothermal procedure to prepare highly uniform bimetallic sulfides as novel cathode materials for RAZBs. Copper-cobalt binary metallic oxides materials possess higher conductivity and larger capacity compared with their mono-metal oxides compounds due to bimetallic synergistic effects and multiple oxidation states. Furthermore, bimetallic sulfide compounds have smaller bond energy and longer bond length than their oxides, leading to less structural damage, faster kinetics of electrochemical reactions, and better stability. The as-prepared Co-Cu bimetallic sulfides show enhanced electrochemical performance due to various valences of Co and Cu as well as the existence of S. As a result, aqueous Zn/$CuCo_2S_4$ battery shows a high specific capacity of 117.4 mAh/g at 4 A/g and a good cycle life of over 8000 cycles. Based on PANa hydrogel electrolytes, a flexible Zn/$CuCo_2S_4$ battery demonstrates excellent cycling stability. This battery can also meet the requirements of electronic devices with different shapes and performs well in extreme environments, such as freezing, drilling, and hammering. This work opens new avenues to obtain high-rate and long-life cathode materials for RAZBs by utilizing the synergistic effects of bimetallic sulfides and provides a new platform for flexible energy storage devices.

Rechargeable aqueous zinc-based batteries are considered to be one of the most promising candidates for lithium ion batteries (LIBs), since zinc has advantages of resource abundance, low cost, no environmental toxicity and a high theoretical gravimetric and volumetric capacity (820 mAh/g and 5855 mAh/cm^3, respectively) [1–4]. Transition metal oxides possess high theoretical capacity, which are widely used in rechargeable aqueous zinc batteries (RAZBs) [5–12], but their poor intrinsic conductivity hampers the fast electron transportation within the electrodes. Additionally, poor conductivity of these cathode materials leads to poor rate capability and stability especially under high current densities [13–16]. Therefore, seeking better electrode materials with good electronic conductivity is significant to improve the electrochemical performance of RAZBs [17–21].

Transition metal oxides, especially Co_3O_4, possess a variety of oxidation states and can carry out rich redox reactions [22,23]. Thus, they always provide higher specific capacity as well as current density [5,6]. However, the poor electric conductivity of electrode materials significantly impedes their practical applications in RAZBs [24,25]. Chemical adulteration is one of the most effective methods to enhance its electrical conductivity, like bimetallic materials [18,26-28]. Compared to Ni oxides and Co oxides, NiCo composites have better electronic conductivity and more redox reaction sites due to the synergistic effect between different metals to form multiple oxidation states, resulting in higher charge/discharge capacity [13,18]. For these reasons, we introduced

* Corresponding author.
E-mail address: lihf@sustech.edu.cn (H. Li).
[1] These authors contributed equally to this work.

https://doi.org/10.1016/j.cclet.2023.108406
1001-8417/

copper, an element with good conductivity and low price, to prepare copper-cobalt composites. On the other hand, some metal sulfides, such as $NiCoS_4$ [29,30], VS_2 [31] and Mo_6S_8 [32], have been used as electrode materials for energy storage devices. As sulfur has a smaller electronegativity than oxygen, transition metal sulfides have smaller bond energy, longer bond length and better electron transport than those of metal oxides. Therefore, sulfides have a more flexible structure, and good electronic conductivity, leading to less structural damage, faster kinetics of electrochemical reactions and better stability [18,33]. For example, $Zn_{0.76}Co_{0.24}S$, has better electronic conductivity and faster charge-transfer rate than its oxide counterparts, leading to longer cycling stability [34].

In this paper, we used a low-cost and facile hydrothermal procedure to prepare $CuCo_2S_4$, which serves as a novel cathode material for RAZBs. Copper-cobalt binary metallic materials possess higher electrochemical conductivity compared with the mono-metal counterparts. In addition, the existence of S atoms can further produce a more flexible crystal structure and alter electron configurations, leading to enhanced conductivity and stability. As a result, $Zn/CuCo_2S_4$ batteries displayed a good discharge capacity of 117.4 mAh/g at a large current density of 4 A/g and a better long-term cycle life (8000 cycles). Besides, the charge and discharge mechanism of the $Zn/CuCo_2S_4$ battery was performed by *in situ* Raman and XPS, which revealed the high reversibility of $CuCo_2S_4$ as cathode material during the charge/discharge process. Finally, a flexible and highly safe $Zn/CuCo_2S_4$ battery was created based on a sodium polyacrylate (PANa) hydrogel electrolyte, demonstrating good cycling stability. It can also meet the requirements of electronic devices with different shapes and can operate well in extreme environments, such as freezing, drilling, weight loading, and hammering. This study inspires exploration of bimetallic sulfides as cathode material for rechargeable alkaline aqueous zinc batteries.

Herein, using a simple hydrothermal method, $CuCo_2S_4$ nanosheets were prepared on carbon cloth (Fig. 1a). Before synthesis, in order to load more materials, the carbon cloth needs to be pretreated. Here, the carbon cloth was handled by nitric acid to introduce O-containing functional groups and increase its hydrophilicity. The pre-treated carbon fiber was immersed into a mixture solution containing $Cu(NO_3)_2{\cdot}6H_2O$, $Co(NO_3)_2{\cdot}6H_2O$ and thiourea. This mixture solution is carried out by hydrothermal reaction at 200 °C for 12 h to receive a homogeneous $CuCu_2S_4$ sample [35,36]. Fig. 1b shows a spinel structure of $CuCo_2S_4$ in which copper ions are filled in tetrahedral locations and cobalt ions are in octahedral positions (Fig. 1b) [36,37]. X-ray diffraction (XRD) pattern suggested that $CuCo_2S_4$ was successfully synthesized on the pretreated carbon cloth surface (Fig. 1c), which exhibited characteristic peaks at 16.45°, 31.39°, 38.12°, 47.44°, 50.25°, and 55.98°, corresponding to (111), (113), (004), (224), (115), and (004) planes of $CuCo_2S_4$ (JCPDS card No. 42–1450) [38,39]. The distinctive peak at 26.3° indicates the carbon cloth support. For comparison, $CuCo_2O_4$ nanosheets were prepared using the same procedure except that thiourea was replaced by urea (Fig. S1 in Supporting information).

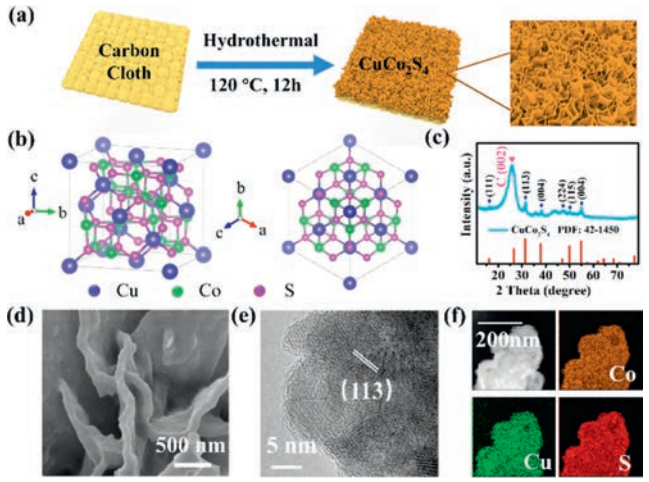

Fig. 1. (a) Schematic diagram of the synthetic route of $CuCo_2S_4$. (b) Two views of the corresponding structure of $CuCo_2S_4$. (c) XRD data of $CuCo_2S_4$. (d) SEM images of $CuCo_2S_4$. (e) TEM of $CuCo_2S_4$. (f) STEM-EDS mapping of $CuCo_2S_4$.

The scanning electron microscopy (SEM) images indicate that highly ordered $CuCo_2S_4$ nanosheets are uniformly dispersed on the good conductive carbon cloth, creating a 3D architectural structure on its surface (Fig. 1d and Fig. S3 in Supporting information). This 3D structure make this material have a large specific surface area and more reaction sites, which may lead to fast and efficient electron transfer during the charge-discharge process. Moreover, the electrolyte could easily penetrate the active material because of its abundant space between the 3D nanosheets. Fig. S2 (Supporting information) displays the SEM data of the $CuCo_2O_4$ nanosheets on the carbon fiber textile surface, which exhibits a resembled morphology resembling that of $CuCo_2S_4$. The detailed morphology of $CuCo_2O_4$ and $CuCo_2S_4$ was further detected by TEM (Fig. 1e and Fig. S4 in Supporting information). In Fig. 1e, the lattice spacing of 2.86 Å could be assigned to the (113) plane of $CuCo_2S_4$. Fig. 1f outlines the elemental composition of $CuCo_2S_4$ through scanning TEM mapping. The corresponding elemental maps of Cu, Co and S present that they are uniformly distributed in $CuCo_2S_4$ (Fig. 1f), as well as in $CuCo_2O_4$ (Fig. S5 in Supporting information).

Using X-ray photoelectron spectroscopy (XPS) characterization, it can be obtained information of elementary composition and oxidation electronic states of $CuCo_2S_4$. XPS spectra show that the as-prepared materials contain Cu, Co and S (Fig. S6a in Supporting information), which is consistent with the above STEM-EDS results. The Cu 2p spectrum in $CuCo_2S_4$ is deconvoluted into two-orbital doubles. The peaks located at 932.2 and 952.0 eV are assigned to Cu^+ species, while those concentrated at 933.1 and 953.6 eV are the characteristics of Cu^{2+} species (Fig. S6b in Supporting information) [40,41]. The Co 2p spectrum in $CuCo_2S_4$ was also fitted with two parts with Co 2p peaks located at 778.5 eV and 793.6 eV indicating the presence of Co^{3+} ions, while that Co^{2+} was at 780.6 eV along with 796.2 eV (Fig. S6c in Supporting information). The peaks at binding energies of 787.0 eV and 802.0 eV represent the corresponding satellite peaks [40,41]. The S 2p spectrum is described at 161.6 eV and 162.8 eV in $CuCo_2S_4$ in Fig. S6d (Supporting information), corresponding to the existence of S^{2-} and the bond of S-O. The peak located at 167.9 eV indicates a high possibility of S reacting with oxygen adsorption on their surface to synthesize sulfite-like compounds [40,41]. The electrochemical performance of $Zn/CuCo_2S_4$ batteries is shown in Fig. 2. The cyclic voltammetry (CV) curves of Zn/CuS, Zn/CoS, $Zn/CuCo_2O_4$ and $Zn/CuCo_2S_4$ batteries at the scan rate of 5 mV/s are presented in Fig. 2a. The $Zn/CuCo_2S_4$ battery indicates the highest current density among them, proving that $CuCo_2S_4$ can exhibit better electrochemical performance than its corresponding oxides (*i.e.*, $CuCo_2O_4$) and monometallic sulfides (*i.e.*, CuS and CoS). In Fig. S7 (Supporting information), the electrochemical impedance spectroscopy (EIS) of the $Zn/CuCo_2S_4$ battery was less than that of the $Zn/CuCo_2O_4$ battery. Fig. 2b presents the CV curves of $Zn/CuCo_2S_4$ batteries at different scan rates ranging from 2 mV/s to 10 mV/s between 0.65–1.95 V. With the increase in scan rates from 2 mV/s to 10 mV/s, the CV profiles are well retained, suggesting excellent reversibility of the $Zn/CuCo_2S_4$ battery. The specific discharge capacities of $CuCo_2O_4$ and $CuCo_2S_4$ are 65 and 117.4 mAh/g at 2 mA/cm^2 (*i.e.*, 4 A/g), respectively (Fig. 2c). The specific capacity of $CuCo_2S_4$ is

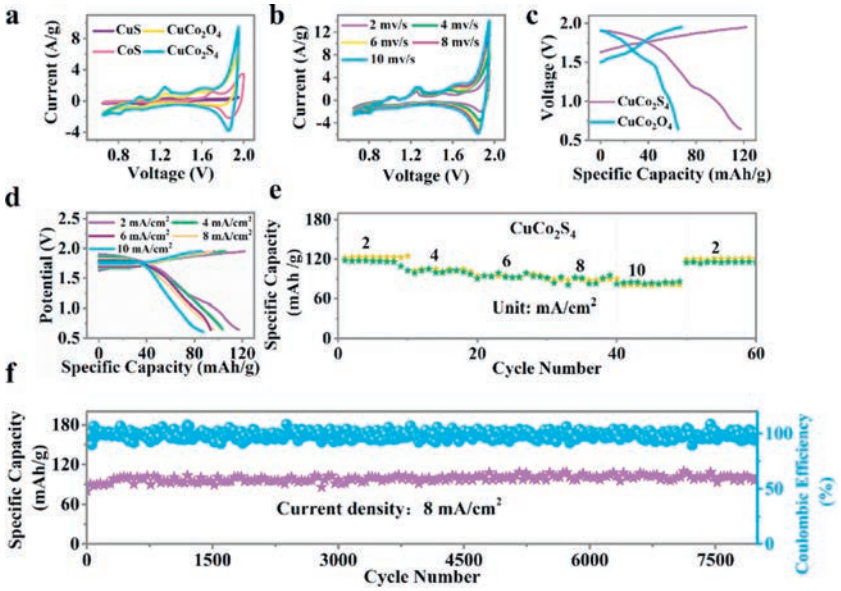

Fig. 2. Electrochemical performances of Zn/$CuCo_2S_4$ batteries in 2 mol/L KOH and 0.02 mol/L $Zn(CH_3COO)_2$ mixture aqueous electrolyte. (a) CV curves of Zn/CuS, Zn/CoS, Zn/$CuCo_2O_4$ and Zn/$CuCo_2S_4$ batteries at the scan rate of 5 mV/s. (b) CV curves of Zn/$CuCo_2S_4$ batteries at different scan rates. (c) The galvanotactic charge and discharge curves of Zn/$CuCo_2O_4$ and Zn/$CuCo_2S_4$ batteries at 2 mA/cm^2 (4 A/g). (d) The galvanotactic charge/discharge curves of Zn/$CuCo_2S_4$ batteries at different current densities. (e) Rate performance of Zn/$CuCo_2S_4$ batteries at different current densities. (f) Cycling performance of Zn/$CuCo_2S_4$ batteries at 8 mA/cm^2 (corresponding to 16 A/g with a mass loading of 0.5 mg/cm^2).

Table 1
Comparison of the key electrochemical performances of some alkaline aqueous zinc batteries.

Batteries	Electrolyte	Working potential (V)	Cycle performance	Ref.
$CuCo_2S_4$//Zn	2 mol/L KOH + 0.02 mol/L $Zn(CH_3COO)_2$	0.65–1.95	111.9% after 8000 cycles	This work
Co_3O_4//Zn	1 mol/L KOH + 0.01 mol/L $Zn(CH_3COO)_2$	1.4–1.93	80% after 2000 cycles	[42]
$NiCoS_4$//porous carbon	2 mol/L KOH	0–1.35	83.4% after 5000 cycles	[29]
Co(III) rich-Co_3O_4//Zn	2 mol/L $ZnSO_4$ + 0.2 mol/L $CoSO_4$	0.8–2.2	92% after 5000 cycles	[24]
VS_2//Zn	1 mol/L $ZnSO_4$	0.4–1.0	98% after 200 cycles	[31]
P–$NiCo_2O_{4-x}$//Zn	1 mol/L KOH + 0.02 mol/L $Zn(CH_3COO)_2$	1.4–1.9	74.2% after 5000 cycles	[18]
NiO/CNT//Zn	1 mol/L KOH + 0.01 mol/L $Zn(CH_3COO)_2$	1.4–1.95	63% after 500 cycles	[43]
Ni foam@Ni_3S_2//Zn	1 mol/L KOH + 0.02 mol/L $Zn(CH_3COO)_2$	1.4–1.9	83.3% after 100 cycles	[44]
CuHCF//Zn	1 mol/L $ZnSO_4$	0–1.1	77% after 20 cycles	[45]
NiCo-DH// Zn	2.5 mol/L KOH + saturated ZnO	1.0–2.0	73% after 850 cycles	[13]
CuHCF//Zn	0.02 mol/L $ZnSO_4$	1.0–2.0	96.3% after 100 cycles	[46]
Mo_6S_8	1.0 mol/L $ZnSO_4$	0.25–1.0	95% after 150 cycles	[32]

almost two times higher than that of $CuCo_2O_4$, indicating that Cu-Co sulfide has a higher capacity than its oxide counterparts. Galvanometer charge/discharge curves under different current densities are displayed in Fig. 2d. The galvanometer discharge capacities of $CuCo_2S_4$ are 117.4, 103.4, 96.1, 93.6, and 87.5 mAh/g at 2, 4, 6, 8, and 10 mA/cm^2, respectively. Fig. 2e presents the rate capability of $CuCo_2S_4$, exhibiting a stable high-rate profile. Fig. 2f illustrates the cycling stability of Zn/$CuCo_2S_4$ batteries at 8 mA/cm^2 (16 A/g). There is an upward trend of the specific discharge capacity of $CuCo_2S_4$ in the first 100 cycles, which then remains almost unchanged. After 8000 cycles, an impressive 111.9% of the initial capacity of $CuCo_2S_4$ (84.0 mAh/g) was achieved, indicating decent cycling stability. It was better than that of $CuCo_2O_4$ (Figs. S8 and S9 in Supporting information).

Furthermore, the Zn/$CuCo_2S_4$ batteries exhibit outstanding electrochemical performance compared to reported sulfides and oxides (Table 1) [13,18,24,29,31,32,42–46]. Fig. S10 (Supporting information) represents the band structure and densities of states of $CuCo_2S_4$, whose band gap is smaller than that of $CuCo_2O_4$. This implies that $CuCo_2S_4$ has more electrons near the Fermi Level and is beneficial for electron transfer. The $CuCo_2S_4$ possesses not only a 3D-nanosheet networked structure, but also has more active sites induced by the interaction of Cu and Co and higher conductivity due to bimetal synergy and the existence of S (Fig. S11 in Supporting information). Thus, $CuCo_2S_4$ can be seen as a promising cathode material in the field of alkaline aqueous zinc batteries.

In order to study the charge and discharge mechanism of the $CuCo_2S_4$ material, *ex-situ* Raman and XPS measurements are described to investigate in Zn/$CuCo_2S_4$ batteries in Fig. 3. In Fig. 3a, it is clear that the typical charge/discharge curves are displayed, which Raman outlined at distinct points A-G (Figs. 3b and c). The peak at 470 cm^{-1} is corresponded to the lattice vibrations (S-S stretching) of Cu-S, while the peaks at 512 cm^{-1} and 673 cm^{-1} are belonged to the Co-S [47–49]. During the charging process (A-C), the peak located at 673 cm^{-1} in the Raman spectra shifts to a lower wavenumber, which corresponds to Co-S, while this peak shifts to a higher wavenumber during the discharging process. With the charging and discharging of the battery, Raman peaks shift gradually and finally go back to their original positions, implying the high reversibility of the as-prepared batteries. Figs. 3d-f demonstrate the *ex-situ* XPS spectra of $CuCo_2S_4$, which further confirm the oxidation state of Co atoms. The peaks located at 778.4 and 793.7 eV of the Co 2p spectra belong to Co^{3+}. Besides, peaks at 780.8 along with 796.6 eV are assigned to Co^{2+}. The proportion of Co^{3+}/Co^{2+} declined slightly from 0.50 to 0.44 during the dis-

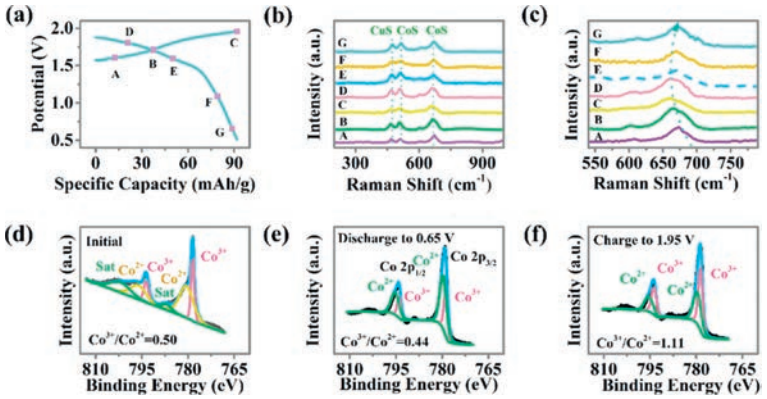

Fig. 3. Electrochemical and structural transformation of $CuCo_2S_4$ during the electrochemical process: (a) The charge/discharge curves for the second cycle at a current density of 8 mA/cm^2 in the 2 mol/L KOH aqueous electrolyte along with 0.02 mol/L $Zn(CH_3COO)_2$. (b, c) The points A–G mark the states where spectra are performed for Raman analysis, high-resolution XPS spectra of Co 2p for (d) initial, (e) discharge to 0.65 V, and (f) charge to 1.95 V.

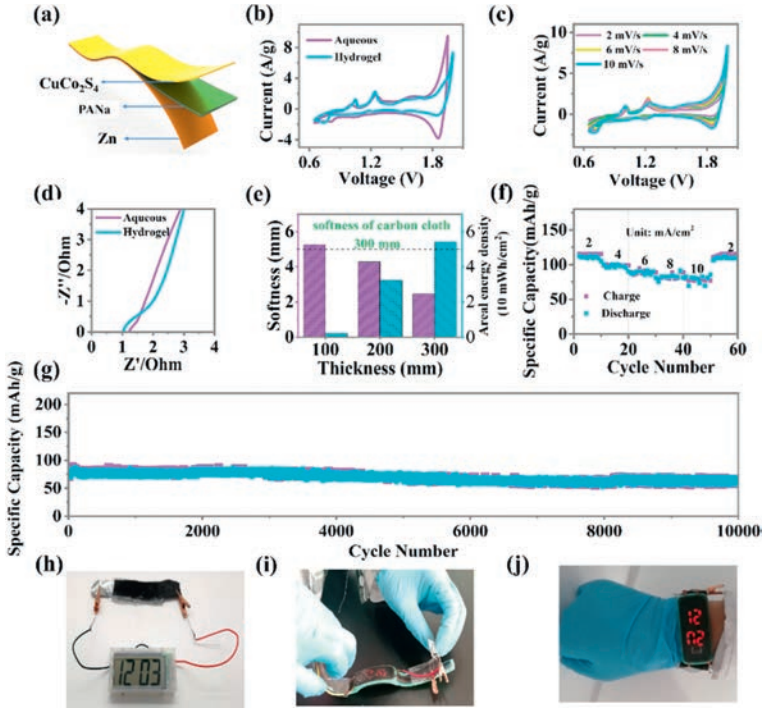

Fig. 4. Electrochemical performance of rechargeable solid-state zinc batteries. (a) Schematic illustration of the structure of the flexible Zn/$CuCo_2S_4$ battery based on PANa hydrogel electrolytes at the scan rate of 5 mV/s. (b) The CV curves of the PANa hydrogel electrolyte and aqueous solution (the 2 mol/L KOH aqueous electrolyte with 0.02 mol/L $Zn(CH_3COO)_2$). (c) The CV curves of Zn/$CuCo_2S_4$ batteries based on PANa hydrogel at various scan sweeps, (d) The AC impedance spectrum of Zn/$CuCo_2S_4$ battery based on PANa hydrogel electrolytes and aqueous solution (the 2 mol/L KOH aqueous electrolyte with 0.02 mol/L $Zn(CH_3COO)_2$ (from 10 kHz to 0.01 Hz). (e) Softness and areal energy density of flexible Zn/$CuCo_2S_4$ batteries constructed with various thicknesses of cathode materials. (f) The rate performance of the flexible Zn/$CuCo_2S_4$ battery. (g) Cycling stability of Zn/$CuCo_2S_4$ batteries with PANa hydrogel electrolytes at 8 mA/cm^2 (or 16 A/g, loading 0.5 mg/cm^2). (h-j) Digital watches powered by flexible Zn batteries.

charge process but increased to 1.1 when the battery was charged to 1.95 V, which matched well with the Raman analysis.

Therefore, the possible electrochemical reactions for $CuCo_2S_4$ and charge/discharge reactions can be summarized as follows [18,50]:

Cathode:

$$CuS + OH^- \leftrightarrow CuSOH + e^- \quad (1)$$

$$CoS + OH^- \leftrightarrow CoSOH + e^- \quad (2)$$

$$CoSOH + OH^- \leftrightarrow CoSO + e^- + H_2O \quad (3)$$

Anode:

$$Zn + 4OH^- \leftrightarrow Zn(OH)_4^{2-} + 2e^- \quad (4)$$

To further investigate the application potential of $CuCo_2S_4$ as cathode materials for flexible and wearable devices, flexible Zn/$CuCo_2S_4$ batteries were created based on the PANa hydrogel. The PANa hydrogel was soaked in a mixture solution of the 2 mol/L KOH aqueous electrolyte along with 0.02 mol/L $Zn(CH_3COO)_2$ to ensure to assimilate a large amount of water and anions, ensuring excellent ionic conductivity [51]. Fig. 4a presents the schematic illustration of the structure of Zn/$CuCo_2S_4$ batteries based on PANa hydrogel electrolytes. According to Fig. 4b, the area of the CV curve of PANa hydrogel electrolyte is slightly smaller than that of KOH mixed aqueous solution. CV profiles of Zn/$CuCo_2S_4$ batteries based on PANa hydrogel were measured at different scan rates ranging from 2 mV/s to 10 mV/s (Fig. 4c). $CuCo_2S_4$ in the PANa hydrogel electrolyte has slightly increased resistance than that of the aqueous solution (Fig. 4d). The ionic conductivity of PANa hydrogel

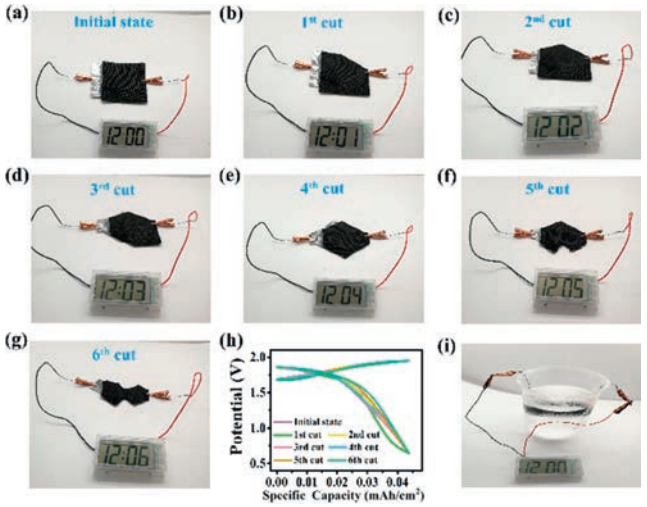

Fig. 5. Cutting test of the flexible Zn/$CuCo_2S_4$ battery based on the PANa hydrogel electrolyte. (a) Initial state, (b) after the first cut, (c) after the second cut, (d) after the third cut, (e) after the fourth cut, (f) after the fifth cut, (g) after the sixth cut. (h) The galvanotactic charge/discharge curves of Zn/$CuCo_2S_4$ batteries at different cutting status, (i) The flexible Zn/$CuCo_2S_4$ battery in freezing test.

electrolyte in this work is 0.1 S/cm. The softness is influenced by the thickness of cathode compounds covered on carbon cloth. The softness and energy density of flexible Zn/$CuCo_2S_4$ batteries with various thicknesses of cathode materials are presented in Fig. 4e. The softness declines as the thickness of active materials increases. Conversely, the areal energy density of the Zn/$CuCo_2S_4$ devices increases with the thickness of active materials. Therefore, the thickness of cathode materials of 200 mm would be optimal, and we used this thickness for our cathode materials. The as-prepared flexible Zn/$CuCo_2S_4$ batteries based on PANa hydrogel electrolytes show good rate capability along with a super-long cycling life of over 10,000 cycles (Figs. 4f and g). Moreover, this sort of flexible Zn/$CuCo_2S_4$ batteries possesses good flexibility which can be utilized to make an energy wristband to power digital watches (Figs. 4h-j).

Flexible Zn/$CuCo_2S_4$ battery based on polymer hydrogel electrolytes can also perform well in various harsh conditions. As shown in Figs. 5a-g, after different cutting times, the flexible Zn/$CuCo_2S_4$ battery can still act as a reliable power source for electronic watches. With the increase in the cutting area, the voltages of the flexible Zn/$CuCo_2S_4$ battery almost remained unchanged (Fig. 5h), demonstrating that this kind of battery can be tailored to meet the requirements of wearable devices with unusual shapes. The charge/discharge curves of Zn/$CuCo_2S_4$ batteries at various cutting status also can show high stability. In addition, this type of battery is suitable for other harsh conditions, such as freezing in ice (−20 °C) (Fig. 5i), drilling, weight loading, and hammering (Fig. S12 in Supporting information). These results show that our flexible Zn/$CuCo_2S_4$ batteries possess high durability and robustness, which can serve as reliable and powerful energy suppliers for wearable devices.

In summary, highly uniform Co-Cu bimetallic sulfides can be considered as excellent cathode materials for rechargeable and flexible zinc batteries. The as-prepared $CuCo_2S_4$ nanosheets present superior discharge capacities of 117.4 mAh/g (4 A/g) and 84.0 mAh/g (16 A/g), which is much higher than corresponding oxides (*i.e.*, $CuCo_2O_4$) and monometallic sulfides (*i.e.*, CuS and CoS). It shows that Cu-Co bimetallic synergy can introduce more active sites, and Cu-Co sulfide can obtain a flexible structure with smaller bond energy and longer bond length, which is beneficial for electron transport. The as-prepared Zn/$CuCo_2S_4$ batteries also demonstrate admirable cycling life with a 111.9% retention rate after 8000 cycles. Besides, flexible Zn/$CuCo_2S_4$ batteries based on PANa hydrogel electrolytes can perform as wearable and reliable power sources, delivering good discharge capacity along with excellent cycle life (over 10,000 cycles). This kind of battery can also be tailored to meet the requirements of wearable devices with unusual shapes and perform well in other destructive conditions, such as freezing, drilling, weight loading, and hammering. This work expands the accessible cathode materials by designing bimetallic sulfides for rechargeable Zn batteries and flexible devices.

Declaration of competing interest

The authors declare that they have no known competing financial interests or personal relationships that could have appeared to influence the work reported in this paper.

Acknowledgments

This research was supported by National Natural Science Foundation of China (No. 22005207), Guangdong Basic and Applied Basic Research Foundation (Nos. 2019A1515011819, 2020A1515110442). The authors also would like to thank Yang Chengyu from Shiyanjia Lab (www.shiyanjia.com) for the TEM analysis.

Supplementary materials

Supplementary material associated with this article can be found, in the online version, at doi:10.1016/j.cclet.2023.108406.

References

[1] Y. An, Y. Tian, C. Liu, et al., ACS Nano 15 (2021) 15259–15273.
[2] X. Wang, B. Xi, X. Ma, et al., Nano Lett. 20 (2020) 2899–2906.
[3] X. Wang, Z. Zhang, B. Xi, et al., ACS Nano 15 (2021) 9244–9272.
[4] Z. Zhang, B. Xi, X. Ma, et al., SusMat 2 (2022) 114–141.
[5] G. Fang, J. Zhou, A. Pan, et al., ACS Energy Lett. 3 (2018) 2480–2501.
[6] A. Konarov, N. Voronina, J.H. Jo, et al., ACS Energy Lett. 3 (2018) 2620–2640.
[7] A.R. Mainar, O. Leonet, M. Bengoechea, et al., Int. J. Energy Res. 40 (2016) 1032–1049.
[8] M. Song, H. Tan, D. Chao, et al., Adv. Funct. Mater. 28 (2018) 1802564.
[9] Y. Niu, D. Wang, Y. Ma, et al., Chin. Chem. Lett. 33 (2022) 1430–1434.
[10] Y. Liu, X. Wu, Chin. Chem. Lett. 33 (2022) 1236–1244.
[11] X. Wang, Z. Zhang, M. Huang, et al., Nano Lett. 22 (2022) 119–127.
[12] Z. Zhang, B. Xi, X. Wang, et al., Adv. Funct. Mater. 31 (2021) 2103070.
[13] H. Chen, Z. Shen, Z. Pan, et al., Adv. Sci. 6 (2019) 1802002.
[14] L.Y. Chen, X.W. Guo, J.H. Han, et al., J. Mater. Chem. A 3 (2015) 3620–3626.
[15] C. Dong, Q. Bai, G. Cheng, et al., RSC Adv. 5 (2015) 6207–6214.
[16] C. Han, H. Li, Y. Li, et al., Nat. Chem. 12 (2021) 2400.
[17] J. Hao, X. Li, S. Zhang, et al., Adv. Funct. Mater. 30 (2020) 2001263.
[18] Y. Zeng, Z. Lai, Y. Han, et al., Adv. Mater. 30 (2018) 1802396.
[19] D. Chao, W. Zhou, C. Ye, et al., Angew. Chem. Int. Ed. 58 (2019) 7823–7828.
[20] T. Sun, Z.J. Li, Y.F. Zhi, et al., Adv. Funct. Mater. 31 (2021) 2010049.
[21] B. Tang, G. Fang, J. Zhou, et al., Nano Energy 51 (2018) 579–587.
[22] Y. Tang, X. Li, H. Lv, et al., Adv. Energy Mater. 10 (2020) 2000892.
[23] M. Cui, X. Bai, J. Zhu, et al., Energy Stor. Mater. 36 (2021) 427–434.
[24] L. Ma, S. Chen, H. Li, et al., Energy Environ. Sci. 11 (2018) 2521–2530.
[25] Q. Wang, X. Liang, D. Yang, et al., RSC Adv. 7 (2017) 29933–29937.
[26] X. Zeng, J. Mao, J. Hao, et al., Adv. Mater. 33 (2021) 2007416.
[27] Y. Zeng, X.F. Lu, S.L. Zhang, et al., Angew. Chem. Int. Ed. 60 (2021) 22189–22194.
[28] J. Ji, H. Wan, B. Zhang, et al., Adv. Energy Mater. 11 (2021) 2003203.
[29] F. Yu, Z. Chang, X. Yuan, et al., J. Mater. Chem. A 6 (2018) 5856–5861.
[30] N. Li, G. Qu, X. Zhang, et al., Chin. Chem. Lett. 33 (2022) 3272–3276.
[31] P. He, M. Yan, G. Zhang, et al., Adv. Energy Mater. 7 (2017) 1601920.
[32] Y. Cheng, L. Luo, L. Zhong, et al., ACS Appl. Mater. Inter. 8 (2016) 13673.
[33] M. Zhang, K.P. Annamalai, L. Liu, et al., RSC Adv. 7 (2017) 20724–20731.
[34] H. Li, Z. Li, M. Sun, et al., Electrochim. Acta 319 (2019) 716–726.
[35] R. Verma, K. R, U.V. Varadaraju, Appl. Surf. Sci. 418 (2017) 30–39.
[36] L. Wu, L. Sun, X. Li, et al., Small 16 (2020) 2001468.
[37] M. Yıldırım, A. Kocyigit, A. Sarilmaz, et al., J. Electron. Mater. 49 (2020) 949–958.
[38] S.E. Moosavifard, S. Fani, M. Rahmanian, Chem. Commun. 52 (2016) 4517–4520.
[39] F. Wang, J. Zheng, G. Li, et al., Mater. Chem. Phys. 215 (2018) 121–126.
[40] S. Cheng, T. Shi, C. Chen, et al., Sci. Rep. 7 (2017) 6681.

[41] T. Zheng, G. Li, X. Meng, et al., Chem. Eur. J. 25 (2018) 885–891.
[42] X. Wang, F. Wang, L. Wang, et al., Adv. Mater. 28 (2016) 4904–4911.
[43] X. Wang, M. Li, Y. Wang, et al., J. Mater. Chem. A 3 (2015) 8280–8283.
[44] P. Hu, T. Wang, J. Zhao, et al., ACS Appl. Mater. Inter. 7 (2015) 26396–26399.
[45] Z. Jia, B. Wang, Y. Wang, Mater. Chem. Phys. 149-150 (2015) 601–606.
[46] R. Trócoli, F. La Mantia, ChemSusChem 8 (2015) 481–485.
[47] L. Chen, R. Lin, C. Yan, Mater. Lett. 235 (2019) 6–10.
[48] L. Nie, H. Wang, Y. Chai, et al., RSC Adv. 6 (2016) 38321–38327.
[49] A.T.A. Ahmed, S.M. Pawar, A.I. Inamdar, et al., Int. J. Energy Res. 44 (2020) 1798–1811.
[50] S. Liu, Y. Yin, K.S. Hui, et al., Adv. Sci. 5 (2018) 1800733.
[51] S. Chen, L. Ma, S. Wu, et al., Adv. Funct. Mater. 30 (2020) 1908945.